

Dynamics of barred galaxies: effects of disk height

Anatoly Klypin^{1,?}, Octavio Valenzuela², Pedro Colin³, and Thomas Quinn⁴

¹Department of Astronomy, New Mexico State University, Las Cruces, NM 88003-0001

²Instituto de Astronomía, Universidad Nacional Autónoma de México, A.P. 70-264, 04510, México, D.F.

³Centro de Radioastronomía y Astrofísica, UNAM, Apartado Postal 72-3 (Xangari), 58089 Morelia, México

⁴Department of Astronomy, University of Washington, Seattle, WA 98195-1580

Accepted 2009 Received August 2008

ABSTRACT

We study dynamics of bars in models of disk galaxies embedded in realistic dark matter halos. We find that disk thickness plays an important, if not dominant, role in the evolution and structure of the bars. We also make extensive numerical tests of different N-body codes used to study bar dynamics. Models with thick disks typically used in this type of modeling (height-to-length ratio $h_z=R_d=0.2$) produce slowly rotating, and very long, bars. In contrast, more realistic thin disks with the same parameters as in our Galaxy ($h_z=R_d=0.1$) produce bars with normal length $R_{\text{bar}}=R_d$, which rotate quickly with the ratio of the corotation radius to the bar radius $R_c=1.2-1.4$ compatible with observations. Bars in these models do not show a tendency to slow down, and may lose as little as 2–3 percent of their angular momentum due to dynamical friction with the dark matter over cosmological time. We attribute the differences between the models to a combined effect of high phase-space density and smaller Jeans mass in the thin disk models, which result in the formation of a dense central bulge. Special attention is paid to numerical effects such as the accuracy of orbital integration, force and mass resolution. Using three N-body codes {Gadget, ART, and Pkdgrav} we find that numerical effects are very important and, if not carefully treated, may produce incorrect and misleading results. Once the simulations are performed with sufficiently small time-steps and with adequate force and mass resolution, all the codes produce nearly the same results: we do not find any systematic deviations between the results obtained with TREE codes (Gadget and Pkdgrav) and with the Adaptive-Mesh-Refinement (ART) code.

Key words: galaxies: kinematics and dynamics | galaxies: evolution | galaxies: halos | methods: N-body simulations

1 INTRODUCTION

Barred galaxies represent a large fraction (65%) of all spiral galaxies (e.g., Eskridge et al. 2000; Sheth et al. 2008). Bars are ubiquitous. They are found in all types of spirals: in large lenticular galaxies (Aguerri et al. 2005), in normal spirals such as our Galaxy (Freudenreich 1998) and M 31 (Athanasoula & Beaton 2006; Beaton et al. 2007), and in dwarf magellanic-type galaxies (Valenzuela et al. 2007). An isolated stellar disk embedded into a dark matter halo spontaneously forms a stellar bar as a result of the development of global disk instabilities (e.g., Binney & Tremaine 1987, Sec. 6.5). Bars continue to be closely scrutinized because of their connection with the dark matter halo (e.g., O’Neill & Dubinski 2003; Holley-Bockelmann et al. 2005; Colin et al. 2006; Athanasoula 2007). Because the bars

rotate inside massive dark matter halos, they lose some fraction of the angular momentum to their halos and tend to slow down with time (Tremaine & Weinberg 1984; Weinberg 1985).

The formation of bars and associated pseudobulges is often considered as an alternative to the hierarchical clustering model (Komendy & Kennicutt 2004). This appears to be incorrect: recent cosmological simulations indicate that the secular bulge formation is a part (not an alternative) of the hierarchical scenario. The simulations of the formation of galaxies in the framework of the standard hierarchical cosmological model indicate that bars form routinely in the course of assembly of halos and galaxies inside them (Mayer et al. 2008; Ceverino 2008). The simulations have a fine resolution of 100 pc and include realistic treatment of gas and stellar feedback, which is important for the survival of a bar. Bars form relatively late: well after the last major merger ($z=1-2$ for normal spiral such as our Milky Way),

? e-mail: aklypin@nmsu.edu

when a collision of gas rich galaxies brings lots of gas with substantial angular momentum to the central disk galaxy. As the disk accretes the cold gas from the halo, it forms a new generation of stars and gets more massive. At some stage, the disk becomes massive enough to become unstable to bar formation. Once the stellar bar forms, it exists for the rest of the age of the Universe.

The cosmological simulations are still in preliminary stages, and it is likely that many results will change as they become more accurate and the treatment of the stellar feedback improves. However, existing cosmological simulations already show us the place and the role of traditional N -body simulations of barred galaxies, which start with an unstable stellar disk. It was not clear whether and how this happens in the real Universe. Now the cosmological hydrodynamic simulations tell us that this is somewhat idealistic, but still a reasonable setup compatible with cosmological models.

Simulations of bars play an important role for understanding the phenomenon of barred galaxies (e.g., Miller 1978; Sellwood 1980; Athanassoula 2003; Valenzuela & Klypin 2003). Numerical models successfully account for many observed features of real barred galaxies (Bureau & Athanassoula 2005; Bureau et al. 2006; Beaton et al. 2007). So, it is very important to assess the accuracy of those simulations. Recent disagreements between results of different research groups (Valenzuela & Klypin 2003; O'Neill & Dubinski 2003; Sellwood & Debattista 2006) prompted us to undertake a careful testing of numerical effects and to compare results obtained with different codes. This type of code testing is routine in cosmological simulations (Frenk et al. 1999; Heitmann et al. 2005, 2007), but it never has been done before for bar dynamics. Testing and comparison of numerical codes is important for validating different numerical models. It was instrumental for development of precision cosmology. It is our goal to make such tests for N -body models of barred galaxies.

We use four different popular N -body codes: ART (Kravtsov et al. 1997), Gadget-1 and Gadget-2 (Springel et al. 2001; Springel 2005), and Pkdgrav (Wadsley et al. 2004). ART is an Adaptive Mesh Refinement code that reaches high resolution by creating small cubic cells in areas of high density. Gadget and Pkdgrav, on the other hand, are TREE codes that compute forces directly for nearby particles and use a multipole expansion for distant ones. We use the codes to run a series of simulations using the same initial conditions for all codes.

We also address another issue: the effects of disk thickness on the structure and evolution of bars. Only recently have the simulations started to have enough mass and force resolution to resolve the vertical height of stellar disks. We use different codes to show that the disk height plays an important and somewhat unexpected role.

One of the contentious issues in the simulations of bar dynamics is the angular speed and the structure of bars in massive dark matter halos. The amount and the rate at which bars slow down is still under debate. Debattista & Sellwood (1998, 2000) find in their massive halo models, i.e., those for which the contributions of the disk and the halo to the mass in the central region are comparable, that the bar loses about 40% of its initial angular momentum, L_z , in 10 Gyr. However, in simulations with much better force resolution and a more real-

istic cosmological halo setup, Valenzuela & Klypin (2003) and Colin et al. (2006) find a decrease in L_z of only 4-8% in 6 Gyr. Debattista & Sellwood (1998, 2000) also find that bars do not significantly slow down for lower density halos.

Valenzuela & Klypin (2003) presented bar models in which stellar disks were embedded in a CDM Milky-Way-type halos with realistic halo concentrations $c \approx 15$, where c is the ratio of the virial radius to the characteristic radius of the dark matter halo. These simulations were run with the ART code with high spatial resolution of 20-40 pc. The bars in the models were rotating fast for billions of years. Valenzuela & Klypin (2003) argued that slow bars in previous simulations were an artifact of low resolution. Sellwood & Debattista (2006) used initial conditions of one of the models of Valenzuela & Klypin (2003) and run a series of simulations using their hybrid, polar-grid code. They found, in most cases, a different evolution than that reported in Valenzuela & Klypin. In particular, contrary to Valenzuela & Klypin's results, they did not find that the bar pattern speed is almost constant for a long period of time. They attribute the differences to the ART refinement scheme.

While Valenzuela & Klypin (2003) mention numerical effects (lack of force and mass resolution) as the cause for excessive slowing down of bars in earlier simulations, there was another effect, which was not noticed by Valenzuela & Klypin (2003): Their disk was rather thin, with a scale-height h_z of only 0.07 of the disk scale-length R_d . This should be compared with $h_z \approx 0.2 R_d$ used in most studies of stellar bars (e.g., Athanassoula & Misirotis 2002; Athanassoula 2003; Martinez-Valpuesta et al. 2006). Models of Debattista & Sellwood (1998) have $h_z = 0.1 R_d$, but the resolution of their simulations was grossly insufficient to resolve this scale. O'Neill & Dubinski (2003) used $h_z = 0.1 R_d$ for a model, which had very little dark matter in the central disk region: $M_{dm} = M_{disk} \approx 1/4$ inside radius $R = 3 R_d$. Dependence of bar speed on disk thickness was noted by Misirotis & Athanassoula (2000): thicker disks result in slower bars.

The remainder of this paper is organized as follows. In section 2 we give a detailed review of available data on disk scale heights and present a simple analytical model for the relation of the disk scale length with the disk scale height. We describe our numerical models in Section 3. In Section 4 we give a brief description of the codes and present analysis of numerical effects. Main results are presented in Section 5. We summarize our results in Section 6.

2 DISK HEIGHTS

Disk scale height appears to play a very important role in the development of barred galaxies. Thus, it is important to know the range of disk scale heights in real spiral galaxies. The most accurate measurement of the disk height comes from the Milky Way galaxy. Edge-on galaxies provide another opportunity to measure disk heights, but those measurements are much less accurate because of dust absorption close to the disk plane. There is not much disagreement between different studies regarding the disk thickness of the Milky Way: the exponential scale height of the stellar thin disk is $h_z \approx 300$ pc (Gilmore & Reid 1983; Ojha et al.

1999; Juric et al. 2008). The thick disk component has a scale height of ~ 1 kpc, but it has a small fraction of mass. Neutral hydrogen and molecular gas have scales 200 pc and 50 pc. So, we can estimate the scale height of the mass distribution as 250–300 pc. Using the exponential disk scale length $R_d \sim 3$ kpc (e.g., Dehnen & Binney 1998a; Klypin et al. 2002), we get the ratio of the scale height to the scale length $h_z = R_d \sim 0.1$.

Observations of edge-on galaxies can be used to estimate the disk heights for other galaxies (e.g., van der Kruit & Searle 1981; Kregel et al. 2002; Bizyaev & Mitronova 2002; Kregel et al. 2005; Yoachim & Dalcanton 2006). Kregel et al. (2005) gave ratios of exponential heights to exponential lengths for 34 edge-on galaxies measured in I-band and found that the median ratio is $h_z = R_d \sim 0.12$. Seth et al. (2005) presents results for brightness profiles in K-band (2MASIS images) for two Milky Way-type galaxies NGC 891 ($V_{\text{max}} = 214$ km/s) and NGC 4565 ($V_{\text{max}} = 227$ km/s). They find the half-light height to exponential disk scale ratios $z_{1/2} = R_d \sim 0.072$ and 0.085 for the two galaxies correspondingly. For the five galaxies in the Yoachim & Dalcanton (2006) sample, which had circular velocities in the range 150–200 km/s, the average ratio was $z_{1/2} = R_d \sim 0.1$.

Estimates of disk heights in edge-on galaxies suffer from substantial absorption close to the plane of the disk (Xilouris et al. 1999; Yoachim & Dalcanton 2006). This makes scale heights of the thin disk difficult to measure directly and causes the results to be dominated by flux coming from high galactic latitudes, where the thick disk is dominant. In turn, this leads to a substantial overestimation (by a factor of 2–3) of the disk heights even in red bands, if one interprets those as estimates of the thin disk component (Yoachim & Dalcanton 2006).

We can use stellar-dynamical arguments to estimate the scale-heights. The idea is to use the ratio of the vertical velocity dispersion σ_z to the radial velocity dispersion σ_R (Kregel et al. 2005). For old main sequence stars ($B - V > 0.5$) in the solar neighborhood, the ratio is measured to be $\sigma_z = \sigma_R \sim 0.5 - 0.6$ (Dehnen & Binney 1998b). We find the same ratio for most of our dynamical model. The vertical velocity dispersion is related to the disk scale-height, and the radial velocity dispersion is related to the disk scale-length (among other parameters of the disk).

Assuming an exponential stellar disk with the vertical density profile $\text{sech}^2(z=h_z)$, one gets:

$$\sigma_R(R) = Q \frac{3.36G(R)}{\kappa(R)}; \quad \sigma_z(R) = G h_z(R); \quad (1)$$

where Q is the Toomre stability parameter; $\Sigma(R)$ is the surface density, and $\kappa(R)$ is the epicycle frequency. For galaxies with flat rotation curves and for radii $R > R_d$ we can use $\sigma_R = \sqrt{2}V_{\text{circ}} = R \dot{\Omega}$. The circular velocity V_{circ} is defined by the mass distribution given by the sum of three components: disk, bulge, and dark matter. It is convenient to parameterize those relative to the total disk mass: $M(R) = M_{\text{disk}} = f_{\text{disk}}(R) + M_{\text{bulge}} = M_{\text{disk}} + M_{\text{dm}}(R) = M_{\text{disk}} X$, where $f_{\text{disk}}(R)$ is the fraction of the disk mass inside radius R . Combining these relations, we get the following expression for the height-to-length ratio:

$$\frac{h_z}{R_d} = \frac{z}{R} \frac{3.36Q}{2} \frac{X^3 \exp(-X)}{f_{\text{disk}}(X) + f_{\text{bulge}} + f_{\text{dm}}(X)}; \quad (2)$$

where $X = R/R_d$, $f_{\text{bulge}} = M_{\text{bulge}}/M_{\text{disk}}$, and $f_{\text{dm}}(X) = M_{\text{dm}}(X)/M_{\text{disk}}$.

We can now estimate the disk height at different radii. For example, we can get it at $R = 3R_d$ assuming that the mass of dark matter is about equal to the disk mass $f_{\text{dm}} = 1$ (Klypin et al. 2002; Willrow et al. 2008) and taking a small bulge $f_{\text{bulge}} = 0.2$. For $Q = 1.5$ (Willrow et al. 2008) and taking $z = R = 0.5$ we get $h_z = 0.11R_d$, which is consistent with the height of Milky Way disk. Eq. (2) gives nearly the same height for $R_d < R < 3R_d$, if we scale the dark matter contribution in such a way that the rotation curve stays constant.

To summarize, the disk scale-heights are relatively small for high surface brightness galaxies such as our Milky Way with $h_z = 0.1R_d$ being a reasonably accurate estimate. Care should be taken not to overinterpret results from edge-on galaxies.

3 MODELS AND SIMULATIONS

3.1 Initial conditions

The setup of initial conditions is described in detail in Valenzuela & Klypin (2003). Here we briefly summarize the most important features. The system of a halo and a disk, with no initial bulge or bar, is generated using the method of Hemquist (1993). In cylindrical coordinates the density of the stellar disk is approximated by the following expression:

$$\rho_d(R; z) = \frac{M_d}{4 h_z R_d^2} e^{-R/R_d} \text{sech}^2 \frac{z}{h_z}; \quad (3)$$

where M_d is the mass of the disk, R_d is the scale length, and h_z is the disk scale height. The latter is assumed to be constant through the disk. The radial and vertical velocity dispersion are given by eqs. (1). Our models keep Q fixed along the disk. The azimuthal velocity and its dispersion are found using the asymptotic drift and the epicycle approximations.

The models assume a NFW density profile (Navarro et al. 1997) for the dark matter halo component, which is described by

$$\rho_{\text{DM}}(r) = \frac{\rho_0}{x(1+x)^2}; \quad x = r/r_s; \quad (4)$$

$$M_{\text{vir}} = 4 \rho_0 r_s^3 \ln(1+c) \frac{c}{1+c}; \quad c = \frac{R_{\text{vir}}}{r_s}; \quad (5)$$

where M_{vir} , R_{vir} , and c are the virial mass, the virial radius, and concentration of the halo, respectively. Given M_{vir} , the virial radius is found once a cosmology is adopted¹. Equations (4–5) of Binney & Tremaine (1987) and the assumption of isotropy in the velocities allow us to determine the radial velocity dispersion as

$$\sigma_{r;\text{DM}}^2 = \frac{1}{M_{\text{DM}}} \int_0^R \frac{GM(r)}{r^2} dr; \quad (6)$$

where $M(r)$ is the mass contained within radius r and G the gravitational constant.

¹ We adopt the flat cosmological model with a non-vanishing cosmological constant with $\Omega_0 = 0.3$ and $h = 0.7$.

Table 1. Initial Parameters of the models

Code	Name	N_{disk} (10^5)	N_{total} (10^6)	N_{eff} (10^6)	Force resolution (pc)	Time-step (10^4 yr)	Disk scale height h_z (pc)
(1)	(2)	(3)	(4)	(5)	(6)	(7)	(8)
K series models: $M_{\text{disk}} = 5 \cdot 10^{10} M_{\odot}$ $M_{\text{tot}} = 1.43 \cdot 10^{12} M_{\odot}$ $R_d = 3.86$ kpc $Q = 1.3$ $c = 10$							
ART	K_{a1}	2.33	2.7	6.6	44	1.4	200
ART	K_{a2}	2.33	2.3	6.6	86	1.9	200
ART	K_{a3}	2.00	2.2	5.9	170	2.2	714
Gadget-1	K_{g1}	1.00	1.1	2.9	280	8.6	714
Gadget-2	K_{g2}	2.33	2.5	6.7	112	2.6	200
Gadget-2	K_{g3}	4.67	5.0	13.8	112	3.3	200
Gadget-2	K_{g4}	2.00	2.2	5.9	140	1.4	200
Gadget-2	K_{g5}	1.00	1.1	2.9	280	29.2	714
Gadget-2	K_{g6}	1.00	1.1	2.9	280	3.6	714
Pkdgrav	K_{p1}	1.00	1.1	2.9	136	24.5	714
Pkdgrav	K_{p2}	2.33	2.5	6.7	136	1.2	200
Model D: $M_{\text{disk}} = 5 \cdot 10^{10} M_{\odot}$ $M_{\text{tot}} = 1.43 \cdot 10^{12} M_{\odot}$ $R_d = 2.57$ kpc $Q = 1.3$ $c = 17$							
Gadget-2	D_{g1}	2.33	2.5	6.7	112	2.6	200

3.2 Description of the models

Selection of parameters of our models is motivated by a number of reasons. First, to simplify the comparison with previous results, we chose parameters, which are close to those used in Colin et al. (2006). Indeed, some of our models have exactly the same parameter as models K_{hb} and D_{cs} in Colin et al. (2006). In this paper we preserve the first letter of the model name (K or D), but use subscripts to identify numerical code. Second, in order to test the effects of the disk height, we construct a new model by taking the K_{hb} model and giving it a larger scale-height $h_z = 714$ pc instead of $h_z = 200$ pc. Third, our models are motivated by predictions of cosmological models. Thus, the models have extended dark matter halos with the NFW profile, realistic virial masses, and concentrations. The central regions of the models are dominated by the disk. The radius at which initially the dark matter mass is equal to the disk mass is equal to 9 kpc for models K and to 6 kpc for models D. Initial profiles of different components are presented in the top two panels of Figure 1 in Colin et al. (2006).

The disk scale-height increases in the course of evolution. We find that for thin disk models it more than doubles after 5 Gyrs of evolution, while for disk thick models the scale-height increases less: by a factor of 1.6. As a result, the scale-height to scale-length ratio of evolved thin disk models is close to the observed $h_z/R_d = 0.1$. The ratio for evolved thick disk models is, on the other hand, twice the observed one.

Table 1 presents the parameters of the models. The first and the second columns give the name of the code and the name of the model. The capital letter of model name represents the model type (K or D). The first subscript in the model name indicates the code used to make the run: a for ART, g for Gadget, and p for Pkdgrav. In columns (3), (4), and (5) we show the disk, the total (disk + dark matter), and the effective number of particles (the number of particles, which we would need, if we used equal-mass particles. The force resolution (6-th column) is twice the smallest cell size for ART code and the spline softening (2.8 times the effective Plummer softening) for tree codes. Note that the force reso-

lution is the distance at which the force accurately matches the Newtonian force. The force continues to increase even below the resolution resulting in large changes in density. Column 7 shows the smallest time-step of simulations. All codes use variable time-steps. Details are given in the next section.

The number of particles inside a sphere of radius equal to the force resolution is quite substantial. For a typical simulation such as K_{a2} or K_{g2} with the resolution 100 pc, there are 100 particles inside the resolution radius at the center of the system at the initial moment. For TREE codes, which keep the resolution constant, the number declines with distance, but it is still large in the plane of the disk. For example, it is 10–15 at 8 kpc. The ART code maintains the nearly constant number of particles inside (increasing) radius of the force resolution at the level of 60 particles (see details in Colin et al. 2006).

Particles with different masses are used in our simulations to increase the mass and force resolution in the central disk region. This is done by placing many small-mass particles in the central disk-dominated region and by utilizing large-mass particles in the outer halo-dominated areas. We use four mass species. The first species represents disk and dark matter particles in the central halo region (the central 40 kpc region). Both the disk particles and the central dark matter particles have the same mass. More massive particles rarely enter the central 10 kpc region. The mass species differ by a factor of two between one species and the next.

The mass resolution (the mass of a disk particle or the mass of the smallest dark matter particle) is given by the ratio of the disk mass to the number of disk particles. It is in the range $m_1 = (1-5) \cdot 10^5 M_{\odot}$. We present the time-step and the initial scale height in the last two columns. The typical number of time-steps for simulations is $(2-4) \cdot 10^5$. The physical parameters of the models, such as the mass of the disk or concentration of the dark matter halo, are shown in separate rows.

In order to estimate the bar pattern speed ω_p we first determine the orientation of the bar by iteratively applying

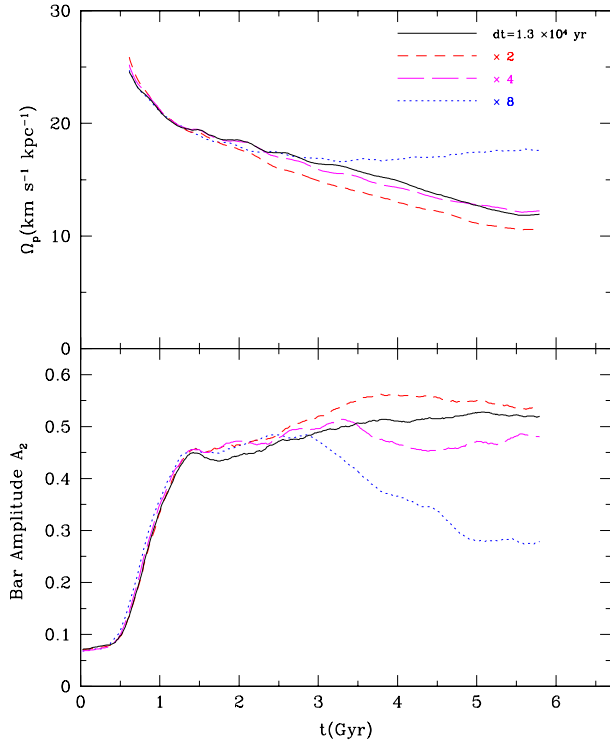


Figure 1. Effects of the time-step on the evolution of bars. The time-step for each model is indicated in the right corner of the top panel. Evolution of the pattern speed of the bar (top panel) and the bar amplitude (lower panel) is shown for a thin disk K model with force resolution 560 pc. Models only start to deviate from each other at the beginning of the buckling phase ($t \approx 2.5$ – 3 Gyr), which is marked by a slight drop in the amplitude of the bar. Once this stage is passed models with sufficiently small time-steps start to converge again except for the run with the largest time-step. We find that the time-step $dt = 10^5$ yrs is not sufficiently small for this model and produces incorrect results.

the method of the inertia tensor in the plane of the disk. $\dot{\rho}_p$ is obtained subsequently by numerical differentiation: $\dot{\rho}_p = d\rho_p/dt$, where ρ_p is the position angle of the bar. In practice, we use about ten consecutive snapshots for which the increasing function ρ_p is available and make a least squares fit. Then $\dot{\rho}_p$ is given by the slope of the straight line. The bar amplitude A_2 is computed similar to Valenzuela & Klypin (2003). For each logarithmically spaced cylindrical bin we find the amplitude of the second Fourier harmonic. Then the amplitude is smoothed over the radius and the maximum is taken as the bar amplitude A_2 . The bar length is defined as out-most radius at which the ratio of axes of isosurface density contours is 1.5. When finding radius of corotation, we use rotational velocity curve of disk particles $V_{rot}(r)$ and find radius, at which it is equal to $\dot{\rho}_p r$.

4 NUMERICAL EFFECTS

4.1 Codes

Simulations were run with three N-body codes: ART (Adaptive Remeshing Tree, Kravtsov et al. 1997), Gadget-1 or Gadget-2 (Springel et al. 2001; Springel 2005), and Pkdgrav (Wadsley et al. 2004). ART is an adaptive mesh re-

meshment (AMR) N-body code, which achieves high spatial resolution by refining the base uniform grid in all high-density regions with an automated refinement algorithm. Gadget is a parallel TREE code. Here we only use the N-body part of the code. Pkdgrav is another TREE code. These two TREE codes differ in the characteristics of the gravitational tree algorithm. For instance, Gadget employs the Barnes & Hut TREE construction (Barnes & Hut 1986) while Pkdgrav uses a binary KD TREE (Bentley 1979). Gadget-2 only uses monopole moments in the multipole expansion while Pkdgrav advocates a hexadecapole as the optimum choice. (Gadget-1 can be configured to use octopole moments). The codes also differ in the cell-opening criterion. Here we use an opening angle criterion $\theta = 0.7$ for Pkdgrav. In the case of Gadget-2 runs we use a tolerance parameter $\epsilon = 0.005$ (see eq.(18) in Springel (2005)). The main advantage of Gadget-2 as compared with Gadget-1 is a more accurate time-stepping scheme (Springel 2005).

The codes use different variants of leapfrog scheme. An algorithm of integration of trajectories can be written as a sequence of operators, which advance particle positions (called drifts) and changes velocities (called kicks). For example, a simple constant-step leapfrog scheme is:

$$v(t_{n+1/2}) = v(t_{n-1/2}) + g(t_n)dt \quad \text{Kick}; \quad (7)$$

$$x(t_{n+1}) = x(t_n) + v(t_{n+1/2})dt \quad \text{Drift}; \quad (8)$$

Thus, the leapfrog integration is a sequence of $K(dt)D(dt)K(dt)D(dt)...$ operators. We call this a KD scheme. Note that the order of operators is not important: the DK scheme is identical to the KD scheme. When the time-step changes with time, the order of operators makes a difference. It is also important to select the moment, at which the time-step should be changed. Following Quinn et al. (1997) we use the operator S to indicate the moment when a new time-step is selected. We also need to specify the time when accelerations (in kicks) and velocities (in drifts) are estimated relative to the moment to which the velocities and coordinates are advanced. We attach the sign '+' ('-') to the name of operator to indicate that the operator uses information from the beginning (end) of the time-step. For example, $K_+(dt)$ is: $v(t_n) = v(t_{n-1}) + g(t_{n-1})dt$ and the operator $D_+(dt)$ is $x(t_n) = x(t_{n-1}) + v(t_n)dt$. Operators with subscript 0 are time symmetric: they use information at the middle of the time-step. Using these operators we can write the algorithms of time-stepping in all our N-body codes:

$$SD_-(dt=2)K_0(dt)D_+(dt=2); \quad \text{Gadget-1} \quad (9)$$

$$SK_-(dt=2)D_0(dt)K_+(dt=2); \quad \text{Gadget-2} \quad (10)$$

$$K_+(dt_1=2)SK_-(dt=2)D_0(dt); \quad \text{ART} \quad (11)$$

$$D_-(dt=2)SK_0(dt)D_+(dt=2); \quad \text{Quinn et al.} \quad (12)$$

The Pkdgrav code has different integration schemes. The scheme given in eqs. (12) uses the algorithm described by Quinn et al. (1997). In our simulations with the Pkdgrav code, we use the scheme which is identical to the Gadget-2 code both in the sense of the sequence of stepping and refinement conditions. This is, in fact, the way Pkdgrav is most commonly run (Wadsley et al. 2004). The ART code uses the time-step dt_1 from previous moment to start the integration. Then, having information on coordinates, it makes a decision on the value of new time-step. The Gadget-2 and

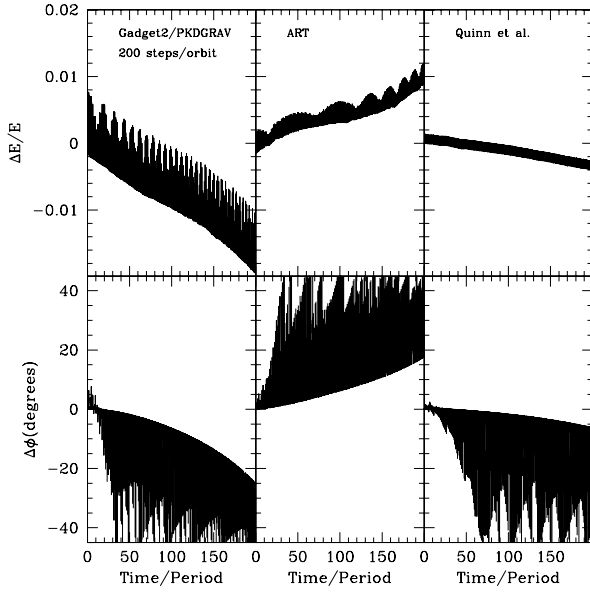


Figure 2. Errors of orbit integration. We integrate trajectory of a particle moving in a gravitational potential created by isothermal distribution of matter $\rho = \log(r)/r^2$. The particle has angular momentum 1/5 of the circular orbit and moves on an elongated orbit with $r_{max} = r_{min} + 10$, which is not unusual for orbits in strong bars. The number of time-steps is 200 per radial period, which corresponds to the time-step of 10^5 yrs when scaled to a realistic galaxy model. The top panels show the error in energy conservation and the bottom ones are the errors in position angle. The left column is for the leap-frog scheme implemented in Gadget-2 and Pkdgrav codes. The middle (right) column is for ART (Quinn et al.) code. The energy conservation is reasonably small, but errors in the orbital angle are unacceptably large.

the ART schemes look different, but actually they are identical, which can be seen when one writes the sequence of a few time-steps. The Gadget-1 and the Quinn et al. schemes look very similar, but they are quite different: the position of the S operator makes the Quinn et al. scheme more accurate (Quinn et al. 1997).

Conditions for changing the time-step are different in different codes. In the ART code the time-step decreases by factor 2 when the number of particles exceeds some specified level (typically 2-4 particles). A cell that exceeds this level is split into eight smaller cells resulting in the drop by 2^3 times of the number of particles in a cell. This prescription gives scaling of the time-step with the local density as $dt \propto \rho^{-1/3}$. Coln et al. (2006) give more details of the procedure. The time-step in Quinn et al. scheme scales as $dt \propto \rho^{-1/2}$. Zemp et al. (2007) also advocate a scheme with this scaling of the time-step. The Gadget and Pkdgrav code use a scaling with the gravitational acceleration $dt \propto g^{-1/2}$, which for $\rho \propto r^{-2}$ gives $dt \propto r^{-1/4}$. Among all the codes the Quinn et al. scheme uses the most aggressive prescription for changing the time-step and Gadget has the smallest change in dt.

In practice, the time-step dt for the Gadget-2 code is defined by parameter

$$dt = \frac{|\mathbf{y} \cdot \mathbf{j}|}{2}; \quad (13)$$

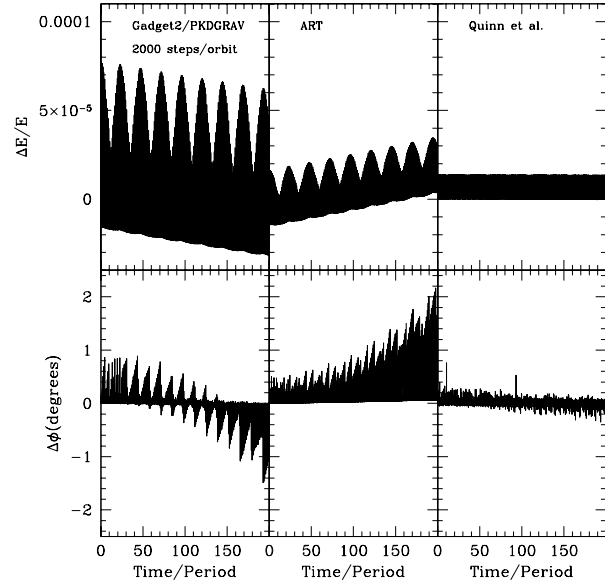


Figure 3. Errors of orbit integration. The same as in Figure 2, but for 2000 time-steps per radial period. This corresponds to a time-step 10^4 yrs in realistic simulations. The errors of integration are very small for both the energy conservation and for the orbital angle.

where $|\mathbf{j}|$ is the acceleration, and ϵ is the effective Plummer softening. For example, we used $\epsilon = 0.04$ for D_{g1} and K_{g2} models. It is $\epsilon = 0.11$ for K_{g1} model. In simulations where we increase the time-step by factor two, we double ϵ . For the Pkdgrav code the time-step is defined by a similar expression: $dt^2 = |\mathbf{y} \cdot \mathbf{j}|^{-2} \epsilon_s$, where ϵ_s is the spline softening. We use $\epsilon_s = 0.025$ for model K_{p2} and $\epsilon_s = 0.050$ for model K_{p1} .

In all codes the time-step changes discretely by factor two: $dt = dt_0 2^{-m}$, where dt_0 is the maximum time-step and m is an integer defined by local conditions (local density or local acceleration).

4.2 Numerical Effects: resolution and time-stepping

In order to obtain accurate results the trajectories of particles should be integrated with a sufficient precision. There is no reliable method of estimating how small a time-step should be. While there are theoretical arguments what integration schemes should (or should not) be used (Quinn et al. 1997; Preto & Tremaine 1999; Springel 2005), only tests can tell how accurate results are. Simulations of bars have a special reason why the orbits should be accurate. Particles, which make up the bar move typically on quite elongated trajectories periodically coming close to the center. When this happens, the acceleration changes substantially, and fast changing accelerations pose problems for numerical integration. If accuracy of integration is not sufficient, a particle may erroneously change its direction of motion and start moving away from the bar. This artificial scattering on the center results in a smaller number of particles staying in the bar. Thus, it is important to have not only accurate particle energies, but also to have accurate phases of trajecto-

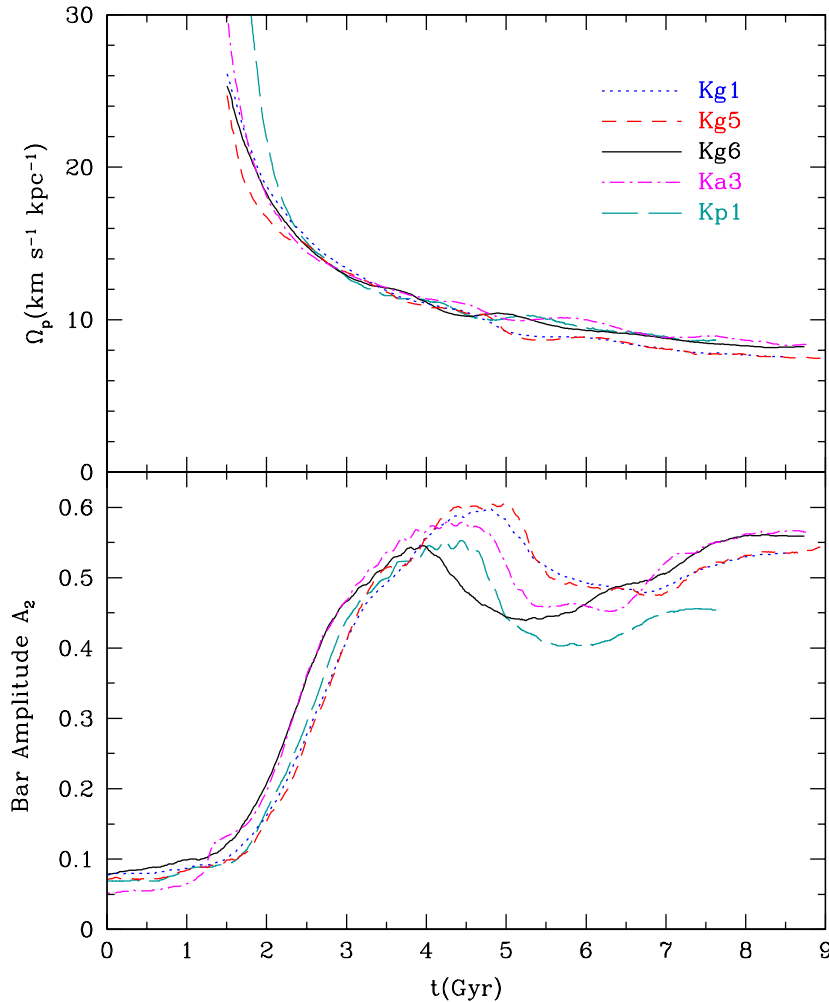


Figure 5. The evolution of the bar pattern speed Ω_p (top panel) and the bar amplitude A_2 (lower panel) for K thick-disk models. All these models evolve similarly: it takes $\approx 2-3$ Gyr to form a bar; the buckling phase happens at $t \approx 5$ Gyr followed by a regime of a constant amplitude and nearly constant pattern speed. Throughout the course of evolution the pattern speed declines by a factor 2-3 and it is very low.

tories. The later is more difficult than the former because different leap-frog schemes used in current N-body codes are known to have problems with accurately tracking orbital phases (e.g., Springel 2005).

The problem is more complicated because there is a real scattering on a dense central region: trajectories have a tendency to get deflected, when they come close to the center. The magnitude of this effect depends on the mass and size of the central concentration. Here the force and mass resolution play an important role. If the resolution is not sufficient, the density in the central region will be lower resulting in less deflection of orbits. Thus, more particles will stay in the bar, which starts to trap even more particles. This leads to excessive growth of the bar.

In order to estimate the effects of time integration on orbits, we start by making simulations of the same model using different time-steps. We use the Gadget-2 code to make simulations of the model K with low force resolution of 560 pc and with $N_{\text{disk}} = 10^5$. The initial disk height is $h_z = 200$ pc.

Figure 1 shows results for simulations with the time-step changing by factor two from one simulation to the other. Overall, we clearly see convergence of the results, but it is not monotonic. Runs with different time-steps evolve very similarly until $2.5(3)$ Gyr, when they start to diverge. The reason for the divergence is likely to be related with the fact that at around $2(3)$ Gyr the system goes through the buckling instability. At this stage the errors in orbit integration produce large errors in the system configuration. For this particular model the time-step of 10^5 yrs was not sufficient: it resulted in a qualitatively wrong answer.

It is difficult to predict what actually happens when the time-step is not small enough. In this case it produced a steep decline in the bar amplitude during the buckling stage. We had the same effect (weakened bar) in ART simulations done with too large time-steps. At the same time, it is quite possible to have just an opposite effect: an artificially stronger bar with lower pattern speed. For example, Sellwood & Debatista (2006) run a model similar to

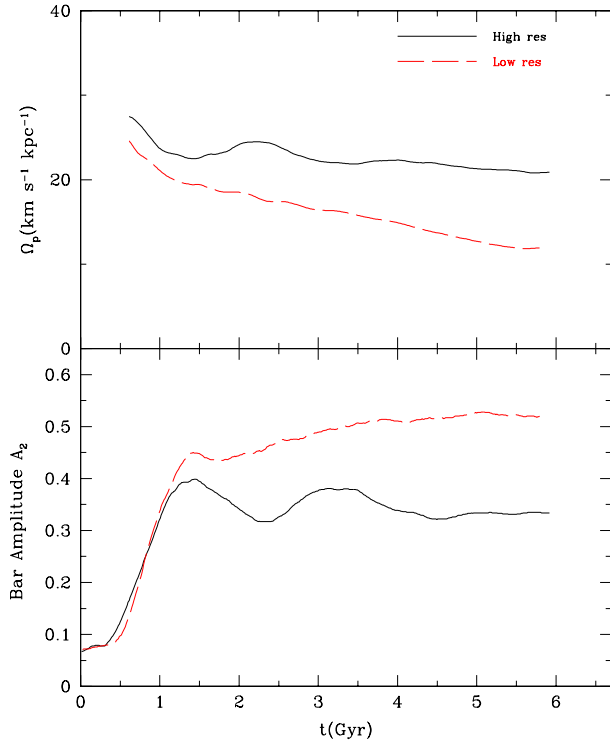


Figure 4. Dependence of bar properties on the force resolution. Evolution of the pattern speed of the bar (top panel) and the bar amplitude (lower panel) are shown for the high resolution model K_{g2} with force resolution 112 pc (full curves) and for a low resolution simulation with 560 pc resolution (dashed curves). The later simulation is the small time-step model presented in Figure 1 with the full curves. Increased force and mass resolution produce a more concentrated bulge, which weakened the bar. A shorter and weaker bar rotates faster and does not slow down much over many billions of years.

K_{g2} with a grossly insufficient time-step $1.5 \cdot 10^5$ yrs; they got a very long and a slow bar. For the same model Valenzuela & Klypin (2003) used a ten times smaller step and got a significantly shorter and faster bar.

The accuracy of orbit integration greatly depends on the distribution of density in the central region: the steeper is the density profile, the more difficult is the simulation. In our case the models K with a thick disk ($h_z = 714$ pc; e.g., runs K_{g5} and K_{a3}) did not form a dense center. We find that for these models a relatively large step of $dt = 10^5$ yrs is sufficient. Models K with thin disk ($h_z = 200$ pc) produce a nearly flat circular velocity curve implying a steep profile, which can be roughly approximated as $v \propto r^{-2}$ in the central 2 kpc region. These models showed inconsistent results when large time-steps $dt > 10^5$ yrs were used. Only when we changed to much smaller steps ($dt = 10^4$ yrs), results became stable.

The observed effect of time-stepping presented in Figure 1 is somewhat unexpected. The most difficult and important part of the simulation is the motion of particles in the central region. Taking a typical particle velocity of 200 km/s we estimate that it would take $2 \cdot 10^7$ yrs and 200 time-steps ($dt = 10^5$ yrs) for a particle to cross the central 2 kpc region. One would expect that 200 time-steps is enough to provide reasonably accurate results. Unfortunately, this is

not the case as Figure 1 shows. Indeed, our simple tests described below indicate that in spite of the fact that the energy is reasonably well preserved, the orbital angle is not conserved: trajectories are scattered very substantially when a large time-step is used. This numerical scattering may result in incorrect properties of the bar.

We investigate the situation with the accuracy of orbit integration by studying the motion of particles in an idealized, but realistic case of a spherical logarithmic potential ($\phi(r) = \log(r)$). We implemented four time-integration schemes used in our simulations: a constant leapfrog scheme, and block-schemes with a variable time-step used in ART, Gadget-2/Pkdgrav, and Quinn et al. codes.

Figure 2 shows the results of integration of an eccentric orbit with the apocenter/pericenter ratio of about 10:1. The gravitational potential is normalized in such a way that the binding energy is equal to the time-averaged kinetic energy. In order to find the accuracy of the orbital angle, we run the orbit with a very small time-step: 10^5 steps per period. Then we find the position angle of a low-accuracy run and compare it with the position angle at the same moment in the small-step run. As compared with a constant-step run, all variable-step integration schemes give smaller errors in the energy conservation, but the errors in the position angle are too large. The constant step run is definitely better, but even in this case the errors ($\sim 10^\circ$) are still large. Decreasing the time-step by factor of ten gives much better results as shown by Figure 3. In this case even the phase of the orbit is accurately simulated. The difference between the ART and the Gadget codes is due to the fact that the ART code takes more small steps in the central part of the orbit (the total number of steps is the same). When we apply the Gadget time-step changing algorithm to the ART code, we get exactly the same results. Quinn et al. takes even more refinements in the center, which improves the accuracy. Yet, the code gives more accurate results even when it runs with the same time-step as Gadget. Still, for a 200 orbits integration (typical for both the bar simulations and for existing cosmological runs) the differences between the codes are not essential. The Quinn et al. scheme wins when we make much longer runs: for 20,000 orbits with 200 step/orbit the Quinn et al. code gave 10 times better accuracy than ART, and GADGET was another factor of ten worse than ART.

A dequate force and mass resolution is another important numerical issue, which is even more difficult to handle. The "converged" (in the sense of time-stepping) solution presented in Figure 1 has a strong bar, which dramatically slows down: the pattern speed declines by a factor of two over 5 Gyr period. Results presented in Figure 4 tell another story: a low-resolution simulation can be very misleading. In this case we use the same thin disk model with twice as many particles and run it with five times better force resolution. The high mass and force resolution simulation is qualitatively different: the bar is weaker and its pattern speed hardly changes.

5 RESULTS

Table 2 gives different properties of the simulated models as measured after 5 Gyr of evolution. In column 2 we present the fraction of the angular momentum lost by the stellar

material. The pattern speed ω_p and the ratio of corotation radius to the bar radius are presented in columns 3 and 4. The bar length is given in column 5. The last three columns give parameters of a double-exponential approximation of the stellar surface density: $\Sigma(r) = \Sigma_{\text{bulge}} \exp(-r/R_{\text{bulge}}) + \Sigma_{\text{disk}} \exp(-r/R_{\text{disk}})$.

The models are clearly split into two groups: those, which started with a thick disk (K_{a3} , K_{g1} , K_{g5} , and K_{p1}) and the models, which started with a thin disk. For example, the ratio of the corotation radius to the bar radius is about 1:7–1:8 for thick disk models. For thin disk models the ratio is visibly smaller: 1:2–1:4. Thin-disk models have shorter bars and less massive bulges. The differences are especially striking when we compare simulations done with the same code and with similar parameters. For example, models K_{a2} and K_{a3} have very similar numerical parameters (time-step, resolution, and number of particles). Yet, their parameters at 5 Gyrs (and actually at any moment) are drastically different. For example, the pattern speed for model K_{a2} is 2.5 times larger than for the model K_{a3} .

5.1 Thick Disk Models

We start with analysis of thick disk K models. It takes $\sim 2-3$ Gyrs to form a bar; the buckling phase happens at ~ 5 Gyrs followed by a regime of a constant amplitude and nearly constant pattern speed. Figure 5 shows the evolution of the bar pattern speed ω_p and the amplitude of the bar A_2 for the models. In Figure 6 we present the total circular velocity profile $V_{\text{tot}}(r) \propto r$, the radial and vertical stellar velocity dispersions, and the disk surface density as a function of distance to the center of the galaxy, R . The comparison is made at 6.5 Gyrs for three models: K_{a3} , K_{g5} , and K_{p1} .

Figure 7 shows disk particles seen along the minor axis of the bar for K models with the thick disk K_{g5} (left panels) and K_{a3} (right panels) at four different epochs. The selected time moments represent different stages of bar evolution. At 4 Gyrs the bar is the strongest, and it has not yet started the buckling stage: the disk is still thin. At 5 Gyrs the system goes through the buckling instability. At this moment the models look different. The differences die out as the buckling instability proceeds. Once the buckling stage is finished, the models again are very close.

Overall, the models evolve very similarly. Some small differences are observed during the buckling phase. Yet, models tend to converge at the end of the evolution. The degree of agreement between different codes as demonstrated by Figure 6 is remarkable. Inside the central 5 kpc region the surface density of the disk deviates from model to model by only few percent. The vertical velocity dispersion over the whole disk deviates not more than 5 km/s.

This agreement between models demonstrates that the results are code independent: if simulations are done with sufficiently small time-steps and with similar force and mass resolution, all codes produce nearly the same results. The results also show that there are no problems with any particular code: all codes produce the same "answer".

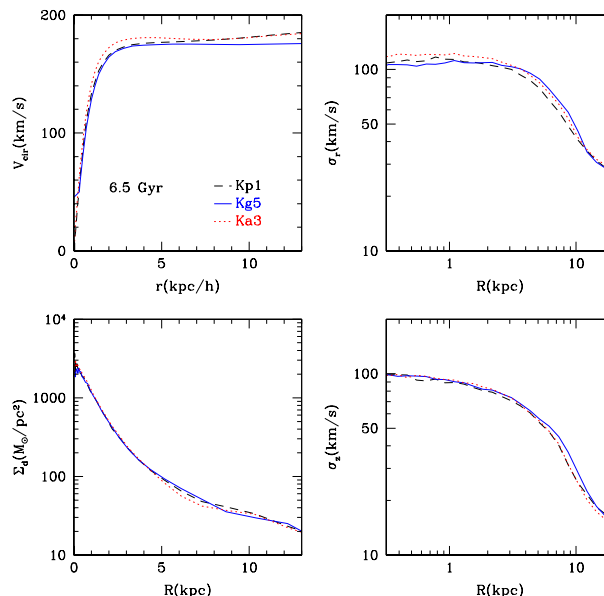


Figure 6. Profiles of total circular velocity (top-left panel), stellar radial and vertical velocity dispersions (top- and bottom-right panel, respectively), and surface density (bottom-left panel) are shown in this four-panel plot for thick-disk K models at 6.5 Gyrs. Here we have selected one model for each code. They agree with each other remarkably well.

5.2 Thin Disk Models

Figures 8 and 9 show the evolution of the bar amplitude and the bar pattern speed for thin disk K models. Again, the simulations behave very similarly, but this time they are very different from the thick disk models K. The thin disk models do not show any substantial evolution in the bar pattern speed and in the bar amplitude. Nevertheless, the agreement between the simulations is not as close as in the case of the thick disk models. It is important to note that there are no systematic differences between results obtained with different codes. The comparison of two runs presented in Figure 9 is especially striking. For example, the Gadget model K_{g2} shows some small decline in the pattern speed and some oscillations in bar pattern speed and bar amplitude. The same evolution of ω_p is demonstrated by the ART model K_{a1} , which also has the oscillations with a slightly larger amplitude. The bar amplitudes for the two models are also very close over the whole simulated period of time. At the same time, models K_{a2} (ART) and K_{g4} (Gadget), which give very similar results, do not show any indication of slowing down of the bar (see Figure 8).

We believe that this agreement between results produced by different codes indicates that there are real physical differences between the models and that those differences are not of numerical origin. In other words, when started with the same physical initial conditions, the evolution produces different results. In the case of the thin disk K models the differences are on the level of 10 percent after 6 Gyrs of evolution.

What are the possible reasons for these variations between the models? The N-body problem is deterministic: initial conditions uniquely define the outcome of evolution. If one starts with identical initial conditions and uses a per-

Table 2. Parameters of the models after 5 Gyrs of evolution

Name	$L=L_b$ (%)	Pattern speed (G yr^{-1})	$R_{\text{cor}}=R_{\text{bar}}$	Bar length R_b (kpc)	Disk scale length R_d (kpc)	Bulge scale length R_{bulge} (kpc)	Bulge/Total
(1)	(2)	(3)	(4)	(5)	(6)	(7)	(8)
Thick disk models							
K_{a3}	9.9	10.0	1.7	10.8	6.7	1.07	0.38
K_{g1}	8.3	10.3	1.7	10.4	7.0	0.97	0.32
K_{g5}	10.3	9.1	1.7	12.1	6.6	1.10	0.36
K_{g6}	8.2	10.5	1.5	11.5	6.5	1.03	0.35
K_{p1}	8.5	10.3	1.8	10.0	6.4	1.00	0.33
Thin disk models							
K_{a1}	5.1	21.0	1.25	6.7	5.7	0.73	0.26
K_{a2}	3.3	25.4	1.16	6.5	5.2	0.54	0.20
K_{g2}	2.7	19.8	1.15	7.5	5.8	0.63	0.23
K_{g3}	2.6	21.7	1.20	6.7	5.3	0.64	0.21
K_{g4}	2.1	22.8	1.22	6.0	5.3	0.61	0.21
K_{p2}	3.1	19.3	1.23	7.4	5.5	0.66	0.22
D_{g1}	10.1	19.5	1.4	7.6	5.2	0.43	0.35

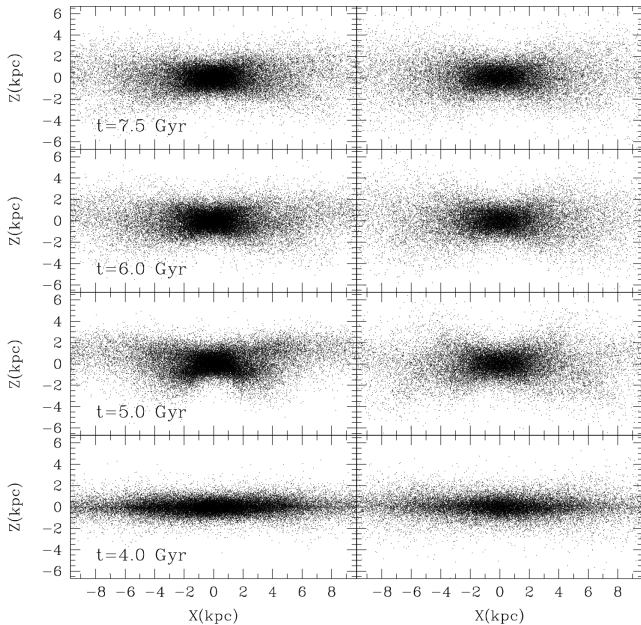


Figure 7. Distribution of disk particles seen along the bar in XZ axis at four different epochs: K_{g5} model (left panels) and K_{a3} model (right panels). Only particles with $|y| < 1.0$ kpc are shown. In order to have similar number of particles in left and right panels only half of the particles, randomly chosen, were used in model K_{a3} . At moment 5 Gyr a bar buckling is clearly seen.

fect code, the results must be unique. Yet, this is too simplistic. An unstable system may have divergent evolutionary tracks. A perturbation slightly changes the system, but because of instabilities, the perturbation grows, and the final answer is different as compared with the evolution of the system without the perturbation. The barred stellar dynamical models have two stages when a system is unstable: the initial stage of formation of the bar and the buckling instability. In addition, even in the quiet periods, the bar itself is an example of a potentially unstable system. For example, it could start trapping more particles resulting in even

stronger bar, which traps even more particles. To large degree, this is exactly what happened with the bars in thick disk K models. The bars were expanding until all the disk became the bar.

The source of perturbations is an interesting issue. In the simulations the perturbations are related with the initial random phases and amplitudes and with numerical inaccuracies. Yet, we should not forget that our models are only approximations to the reality. In real galaxies there is no shortage of perturbations including satellite galaxies and molecular clouds to name the few. Whatever is the source of perturbations, simulations of the same physical model evolve slightly different and produce slightly different results. This is exactly what the thin disk models did.

5.3 Effects of the phase-space density: thin versus thick disks

The only difference in the initial conditions between the thin disk and thick disk K models is the disk scale height. All the other parameters are the same. These seemingly minor variations in initial conditions resulted in a remarkably different evolution and in large differences in the structure of the evolved models. In order to highlight the differences, Figure 10 shows the angular momentum loss $L=L_b$ of the stellar disk and the bar pattern speed for two models run with the Gadget code: one with a thin disk (K_{g3}) and another with a thick disk (K_{g5}). The disk in the thick disk model loses four times more angular momentum and its bar rotates 2.5 times slower as compared with the thin disk model. The dark matter is the same in both models, and it cannot be the reason of the difference.

So, what are the possible reasons for such a large effect of the disk height? The thickness of the stellar disk affects the vertical waves and oscillations (Merritt & Sellwood 1994). This effect is definitely present and will have some impact on the evolution. At the same time, those vertical modes are likely to play a significant role during the buckling stage (Merritt & Sellwood 1994). However, the differences between the models develop too early and they are

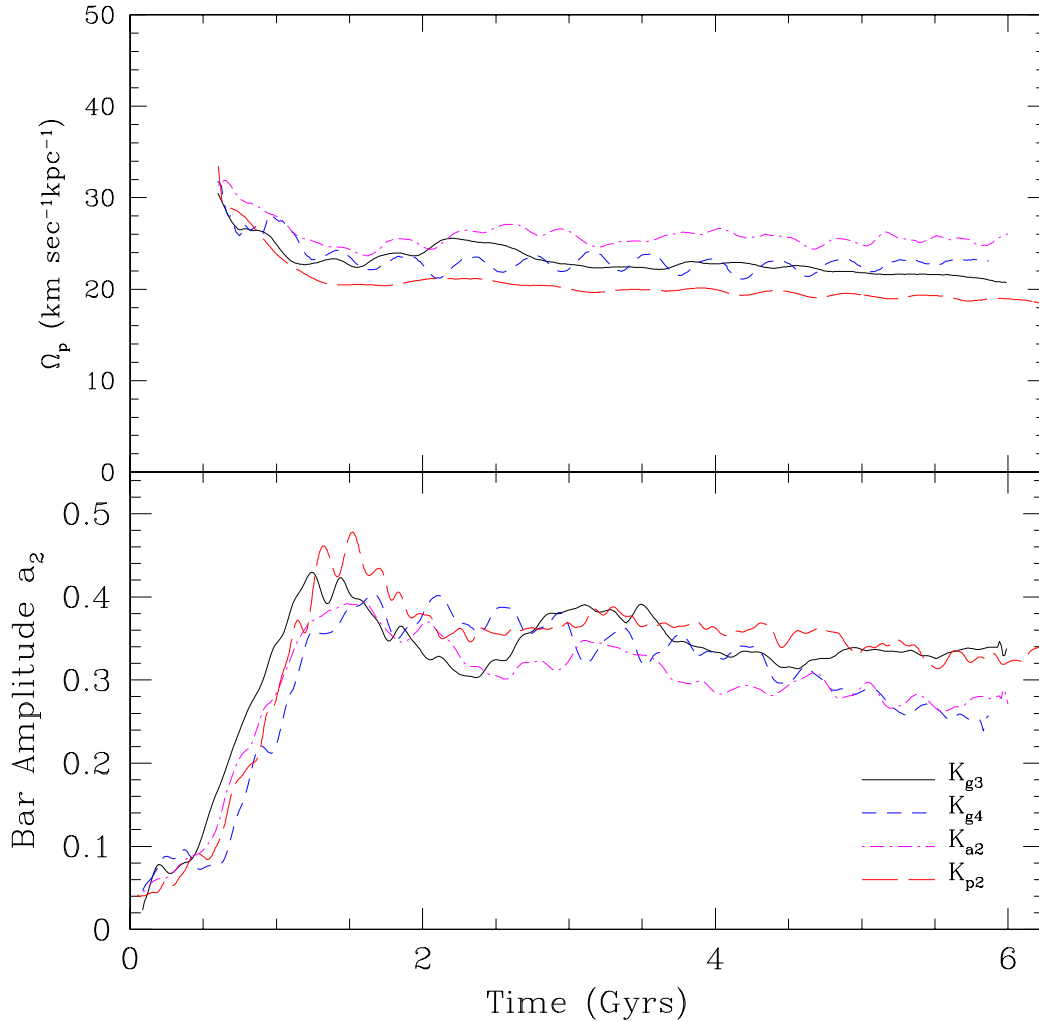


Figure 8. The evolution of the bar pattern speed (top panel) and of the bar amplitude (lower panel) for thin-disk K models made with the Gadget-2, the ART, and the Pkdgrav codes. All the models show pattern speeds Ω_p , which do not show a systematic decline with time. There are differences between different runs, but they are relatively small: $\Omega_p = (21.6 \pm 3) \text{Gyr}^{-1}$. Note substantial differences with respect to the thick-disk models presented in Figure 5.

too large for the vertical modes to be the culprit. In the absence of a reliable theory of stellar bars, one can only speculate what is going on. One may think about two other effects, which can influence the systems: the Jeans mass and the phase-space density. The random velocities, which define the Jeans mass, tend to prevent collapse of perturbations on small scales. Thus, for the same random velocities, larger Jeans masses imply smaller densities. The phase-space density acts in the same way. Thus, we expect that models with higher phase-space density (or smaller Jeans mass) will result in denser and more compact central region, which affects the growth of bars in a profound way.

For a fixed surface density the vertical disk height h_z changes the density in the disk $\propto h_z^{-1}$ and the velocity dispersion $\sigma_z^2 \propto h_z$ (see eq.(2)). Assuming for simplicity that the Jeans mass scales with the velocities and density as $M_J \propto \sigma_z^3 / \rho = \sigma_z^3 / h_z^{-1}$, we get $M_J \propto h_z^4$, which is a remarkably strong effect considering that in our models h_z varies by factor 3.5. The phase-space density changes even more:

$f = \sigma_R \sigma_z / h_z^{3=2}$. For our thin/thick models this gives variations by factor 7.

The Jeans mass affects the evolution in a similar way as the Toomre stability parameter Q : larger Q results in later formation of the bar and in less prominent spiral arms. Comparison of the initial stages of bar formation in Figures 5 and 8 shows the effect: larger h_z (thus, larger σ_z) results in much delayed formation of the bar.

The phase-space density is a complicated quantity, which in practice is used in the form of a coarse-grained phase-space density. Avila-Reese et al. (2005) present detailed results on the evolution of the phase-space density during the formation and evolution of barred disk models. As the system evolves, the coarse-grained phase-space density $f = \sigma_R \sigma_z$ decreases. The phase-space density f can be considered as a measure of the degree of compressibility of a gravitational system: for given rms velocities it defines the real-space density: $\rho = f \sigma_R \sigma_z$. The larger is the phase-space density, the larger is ρ . In turn, the den-

Table 3. Comparison of Parameters of the Milky Way and the model K_{g3}

Parameter	K_{g3}	Milky Way	Reference
Circular velocity (km/s)	220	210-230	Binney & Merrifield (1998, Sec.10.6)
Surface disk density at R ($M_{\odot} \text{pc}^{-2}$)	44.6	48-9	Kuijken & Gilmore (1991)
Vertical rms velocity of stars at R (km/s)	14	15-20	Dehnen & Binney (1998b)
Radial rms velocity of stars at R (km/s)	38	35-40	Dehnen & Binney (1998b)
Pattern Speed Ω_p (km/s/kpc)	50	53-3	Dehnen (1999)
Bar length (kpc)	3.3	3.0-3.5	Freudenreich (1998)
Total mass inside 60 kpc ($10^{11} M_{\odot}$)	5.5	4-0:7	Xue et al. (2008)
Total mass inside 100 kpc ($10^{11} M_{\odot}$)	7.3	7-2:5	Dehnen & Binney (1998a)

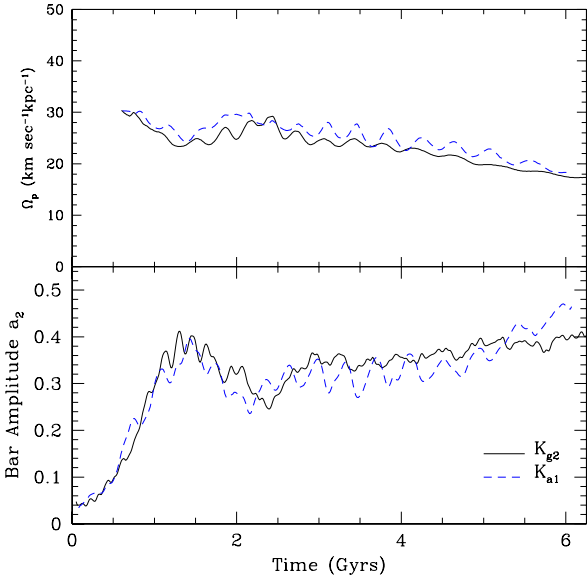


Figure 9. The evolution of the bar pattern speed (top panel) and of the bar amplitude (lower panel) for thin-disk models K_{g2} (Gadget-2) and K_{a1} (ART). These two simulations were performed with different codes, yet they produce very similar results.

sity in the central region of a bar is an important factor because according to our results it moderates the growth of the bar and can prevent it from growing excessively. Thus, the phase-space density in the central disk region is a fundamental parameter, which significantly affects the evolution of barred galaxies.

Indeed, the buildup of mass in the high phase-space density models happens in the models. Figure 11 shows the total (stellar plus dark matter) circular velocity (top-panel) and the stellar surface density (bottom-panel) profiles after 4 Gyr of evolution. We see that the model K_{g2} (thin disk) has a larger inner circular velocity and a larger surface density as compared with the low phase-space density model K_{g5} . The rms velocities (right panels) are nearly the same for the two models. Thus, the K_{g2} model has a substantially larger (by a factor of four) phase-space density. It started with a larger f and it ended with a larger f .

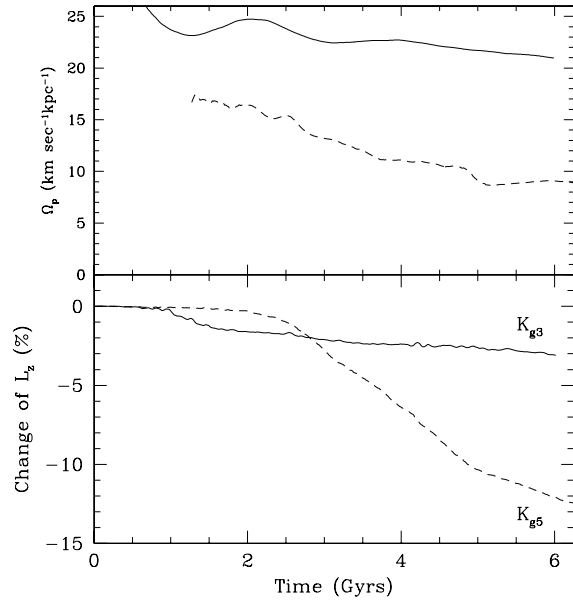


Figure 10. Effects of the initial phase-space density: the evolution of the pattern speed (top panel) and the disk angular momentum loss (bottom panel) for model K_{g3} (full curves) and model K_{g5} (dashed curves). These two models differ by the initial value of the scale height of the disk, which results in substantially different phase-space density. The thin model goes through the buckling instability earlier and has a smaller angular momentum loss.

6 DISCUSSION AND CONCLUSIONS

We find that numerical effects { the mass and force resolution, and the time integration of trajectories } can significantly alter results of simulations. The time-step of integration must be small enough to allow accurate integration of expected trajectories. Acuracy of energy conservation can give a misleading impression that the simulation is adequate, while it actually makes substantial errors in position of orbits. Our experiments with realistic orbits in models with flat rotation curves indicate that even the best available integration schemes require 2000 time-steps per orbit. This requirement is valid for variable-step schemes with more steps required for a constant-step schemes. Numerical tests with full-scale dynamical models confirm the condition. This condition results in very small time-steps of $dt = 10^4$ yrs. If one uses dimensionless units defined by scaling $G = 1$, $M_{\text{disk}} = 1$, $R_d = 1$, then the dimensionless time step should be $dt = 5 \cdot 10^4$. This should be compared with typically

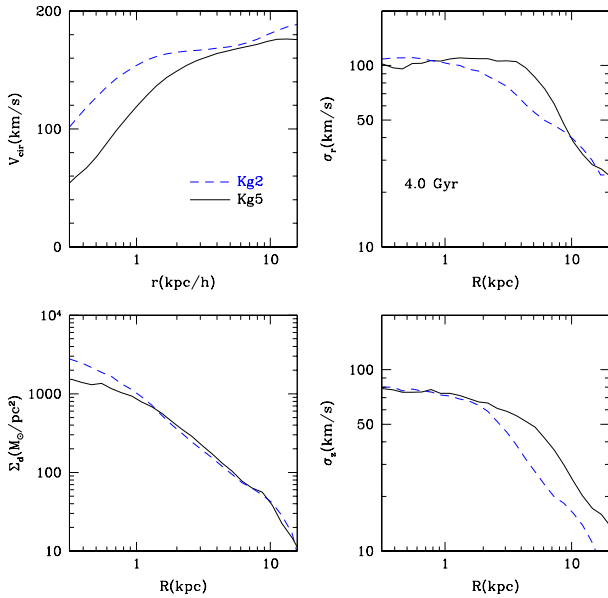


Figure 11. Comparison of profiles of models with different initial phase-space density. The circular velocity (top-left panel), the stellar radial and vertical velocity dispersions (top- and bottom-right panel, respectively), and the surface density (bottom-left panel), as a function of radius for models K_{g2} and K_{g5} , thin and thick disk model, respectively. The comparison is made at 4 Gyr. The thin disk model (dashed curves) evolves to a more concentrated structure. The central concentration explains why the bar pattern speed for this model is higher than in the thick disk model.

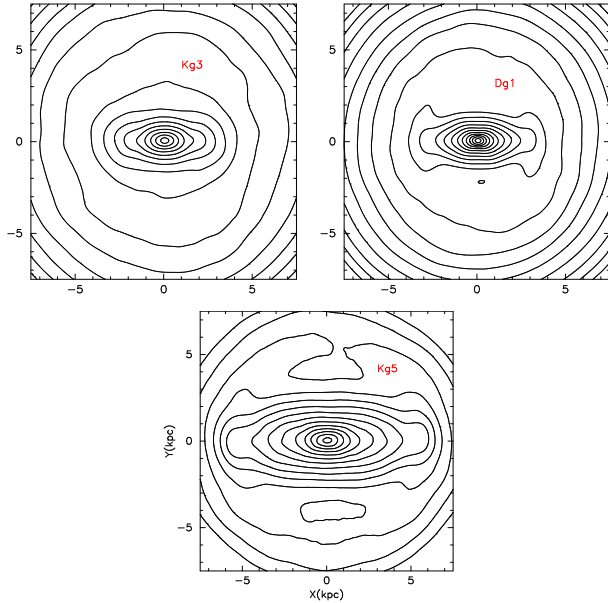


Figure 12. The iso-contours of the surface stellar density for representative models. The thin disk models K_{g3} and D_{g1} develop realistic bars with the ratio of corotation radius to the bar length $R = 1:2$ (left panel; $R_{cor} = 4:5$ kpc) and $R = 1:4$ (right panel; $R_{cor} = 6:1$ kpc). The thick disk model K_{g5} (bottom panel) has a bar, that covers the whole disk with the corotation radius 9.3 kpc. Distances in the plot are given in kpc units. All the models are re-scaled to have the disk scale length 3 kpc (the same as for the Milky Way galaxy).

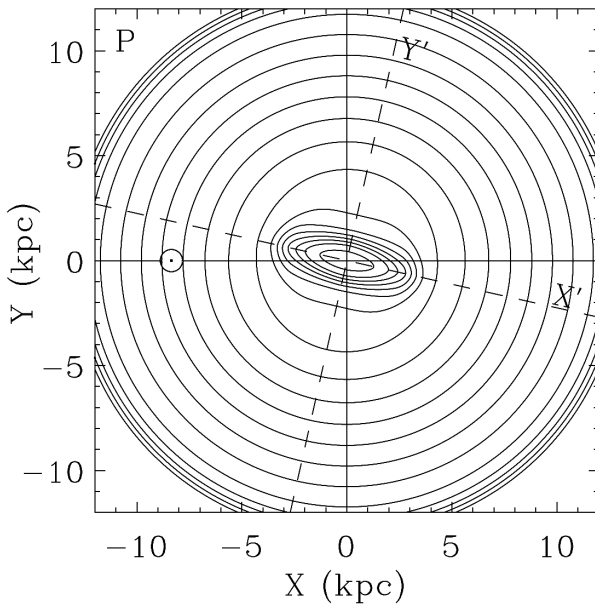
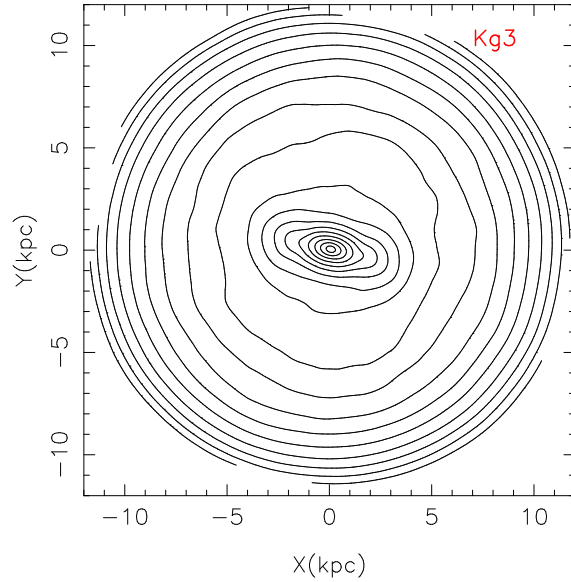


Figure 13. The iso-contours of the surface stellar density for model K_{g3} (top panel) and the Milky Way galaxy (bottom panel). The K_{g3} model was re-scaled to have the evolved disk scale length 3 kpc, which is close to the scale length of our Galaxy. The bottom panel shows one of the models from Freudreich (1998, fig. 14, right panel). The model represents a multi-parameter fit to the COBE DIRBE maps of the near-infrared light coming from central regions of our Galaxy. The small circle shows the position of the Sun. The K_{g3} model reproduces the length and the flattening of the Milky Way bar.

used $dt = 0.01$ (e.g., Athanassoula & Misirotis 2002). This time-step would be insufficient for integration of models with central mass concentration presented in this paper². A constant time-step $dt = 5 \cdot 10^5$ yrs used by Willrow et al. (2008)

² Models studied by Athanassoula & Misirotis (2002) are less concentrated and do not require a small time-step.

is too large for models of the Milky Way galaxy studied in their paper.

The mass and related with it the force resolution also play important role. As Figure 4 shows, a low force resolution produces a less dense central region, which results in a long and a very massive bar. The same model run with better force resolution produces a shorter, less massive, and faster rotating bar.

Once the necessary numerical conditions are fulfilled, the codes produce practically the same results. We do not find any systematic deviations between the results obtained with TREE codes (Gadget and Pkdragv) and with the Adaptive-Mesh-Refinement (ART) code.

Disk height is an important parameter, which is often ignored in models of barred galaxies. In the models, which we consider in this paper, the disk height determines the global properties of the bars. Figure 12 shows surface density maps of the models with different initial disk thickness. Models with thin disks produce short bars with $R_{\text{bar}} \approx R_d$, which rotate relatively fast: $\Omega = 1.2 - 1.4$ and which show very little decline of the pattern speed. Models with thick disk produce long and slow rotating bar. In order to facilitate the comparison with the our Galaxy, we re-scaled models to have the evolved disk scale length 2.65 kpc and to have the circular velocity at the solar distance 220 km/s. Any N-body system has two arbitrary scaling factors, which can be used to scale the system.

Having scaled the models to the disk scale length, we can compare other parameters of the models. Because the simulations with thin disks produce reasonable models, we use one of the models (K_{g3}) and compare it with the Milky Way. Table 3 gives a list of some parameters. Figure 13 compares the surface density maps of the Milky Way (Freudenreich 1998) and the K_{g3} model. These comparisons show that the model fits the Milky Way reasonably well.

We suggest that the disk height is only an indicator of a more fundamental property (the phase-space density in the central ($R < R_d$) region. In our models the phase-space density is uniquely related with the disk height. Initially in our models the disk height is low and the stability parameter $Q = 1.3 - 1.8$ is constant across the disk. Thus, the phase-space density in the central region is high, and subsequent evolution brings that highly compressible stellar fluid close to the center, where it forms a nearly flat circular velocity curve. The later, as we speculate, is responsible for arresting the growth of the bar. This relation between the disk height and the central phase-space density may not be true in general case. For example, O'Neill & Dubinski (2003) and Widrow et al. (2008) consider models with large central Q and, thus, with a low central phase-space density. Indeed, in their models bars slow down substantially.

The nearly constant pattern speed of bars in the thin disk models is somewhat puzzling. A bar is a very massive non-axisymmetric object, which rotates inside a non-rotating dark matter halo. As such, one might expect that it should experience dynamical friction and slow down. This is why results of Valenzuela & Klypin (2003), which showed models with little slowing down of bars, were met with skepticism. Simulations presented in this paper confirm the findings of Valenzuela & Klypin (2003) and show that they cannot be related with numerical problems.

Orbital resonances may be responsible for the observed

slow dynamical friction. The resonances in barred galaxies have been extensively studied in recent years using N-body simulations (e.g., Athanassoula 2003; Colin et al. 2006; Ceverino & Klypin 2007; Weinberg & Katz 2007). It is now well established that a large fraction of stellar particles are in resonance with the bar. Some fraction of dark matter particles are also in resonance (Colin et al. 2006; Ceverino & Klypin 2007), and these are very important for the dynamical friction between the stellar bar and the dark matter.

There are two types of (exact) resonances in an autonomous Hamiltonian dynamical system: elliptic and hyperbolic (Arnold & Avez 1968). Orbits, which are close to an elliptic resonance librate around the exact resonance and have the structure of a simple pendulum (Lichtenberg & Leiberman 1983, Sec.2.4), (Murray & Dermott 1999, Sec. 8). Hyperbolic resonances are points on intersections of separatrices, which separate domains of elliptical resonances. Orbits close to a hyperbolic resonance are unstable and tend to migrate away from the resonance, while orbits close to an elliptical resonance are stable.

Ceverino & Klypin (2007) study in detail the resonant orbits in simulations of barred galaxies. It appears that the orbits belong to elliptical resonances. These orbits track their resonance: the orbits do not evolve if the resonance does not move, and they follow the resonances if it gradually migrates in the phase space. Thus, the elliptical resonances trap the orbits: if an orbit for whatever reason happens to appear in the domain of the resonance, it will have a tendency to stay with the resonance. This phenomenon is thought to be common in Solar System dynamics (e.g., Malhotra 1993). Resonance trapping explains why the simulations show maxima in the distribution of orbital frequencies at the positions of resonances.

Colin et al. (2006) investigate another aspect of the resonant interaction between the stellar bar and the dark matter. They found that the dark matter particles, which are in resonance with the stellar bar, themselves form a bar, which rotates with the same angular speed and has a very small lag angle ($\approx 10^\circ$) as compared with the stellar bar. Colin et al. (2006) argue that the interaction between the dark matter and the stellar bars is the main mechanism for the dynamical friction between the disk and the dark matter. The near alignment of the dark matter and stellar bars means that their interaction is minimized by the resonances.

These results indicate that the resonant interaction between the stellar bar and the dark matter is mostly due to elliptical resonances, and, thus, has a tendency to minimize the transfer of the angular momentum from the disk to the dark matter. Following orbits in such resonances emphasizes the need for conservative time-steps in N-body simulations. Also subtle changes in the underlying global potential could change the relative number of orbits in these resonances leading to disparate results for the slowing of the bar.

ACKNOWLEDGMENTS

P.C. acknowledges support from the DGAPA-UNAM grant IN112806. A.K. acknowledges support by NSF grants to NMSU. T.Q. acknowledges support by NSF ITR grant PHY-

0205413.O.V. thanks support from a CONACYT Repatriation Fellowship. Some of the simulations presented in this paper were performed on the HP CP 4000 cluster (Kambalam) at DGS CA-UNAM, on the Columbia computer at the NASA Ames center, and at the Arctic Region Supercomputing Center.

REFERENCES

- Aguerri, J. A. L., Elias-Rosa, N., Corsini, E. M., & Muñoz-Turoso, C. 2005, *A & A*, 434, 109
- A mold, V. J. & Avez, A. 1968, *Ergodic problems of classical Mechanics*, W. A. Benjamin, Inc.
- Athanassoula, E., & Misiriotis, A. 2002, *MNRAS*, 330, 35
- Athanassoula, E. 2003, *MNRAS*, 341, 1179
- Athanassoula, E., & Beaton, R. L. 2006, *MNRAS*, 370, 1499
- Athanassoula, E. 2007, *MNRAS*, 377, 1569
- Avila-Reese, V., Carrillo, A., Valenzuela, O., & Klypin, A. 2005, *MNRAS*, 361, 997
- Barnes, J., & Hut, P. 1986, *Nature*, 324, 446
- Beaton, R. L., et al. 2007, *ApJ Lett.*, 658, L91
- Binney, J., & Merrifield, M. 1998, *Galactic astronomy / James Binney and Michael Merrifield*. Princeton, NJ : Princeton University Press, 1998.
- Bizyaev, D., & Mitronova, S. 2002, *A & A*, 389, 795
- Bureau, M., & Athanassoula, E. 2005, *ApJ*, 626, 159
- Bureau, M., Aronica, G., Athanassoula, E., Dettmar, R.-J., Bosma, A., & Freeman, K. C. 2006, *MNRAS*, 370, 753
- Binney, J., & Tremaine, S. 1987, *Galactic Dynamics*. Princeton Univ. Press, Princeton, NJ
- Bentley, L. 1979. *IEEE Transactions on Software Engineering* SE-5 4, 333
- Ceverino, D., 2008, private communication
- Ceverino, D., & Klypin, A. 2007, *MNRAS*, 379, 1155
- Coln, P., Valenzuela, O., & Klypin, A. 2006, 644, 687
- Debattista V. P., & Sellwood J. A. 1998, *ApJ*, 493, L5
- Debattista, V. P., & Sellwood, J. A. 2000, *ApJ*, 543, 704
- Dehnen, W., & Binney, J. 1998, *MNRAS*, 294, 429
- Dehnen, W., & Binney, J. J. 1998, *MNRAS*, 298, 387
- Dehnen, W. 1999, *ApJ Lett.*, 524, L35
- Eskridge, P. B., et al. 2000, *AJ*, 119, 536
- Frenk, C. S., et al. 1999, *ApJ*, 525, 554
- Freudenreich, H. T. 1998, *ApJ*, 492, 495
- Gilmore, G., & Reid, N. 1983, *MNRAS*, 202, 1025
- Heimann, K., Ricker, P. M., Warren, M. S., & Habib, S. 2005, *ApJ Suppl.*, 160, 28
- Heimann, K., et al. 2007, *ArXiv e-prints*, 706, arXiv:0706.1270
- Hemquist, L. 1993, *ApJ Suppl.*, 86, 389
- Holley-Bockelmann, K., Weinberg, M. D., & Katz, N. 2005, *ApJ*, 363, 991
- Juric, M., et al. 2008, *ApJ*, 673, 864
- Klypin, A., Zhao, H., & Somerville, R. S. 2002, *ApJ*, 573, 597
- Kormendy, J., & Kennicutt, R. C., Jr. 2004, *ARA & A*, 42, 603
- Kravtsov, A. V., Klypin, A. A., & Khokhlov, A. M., 1997, *ApJ Suppl.*, 111, 73
- Kregel, M., van der Kruit, P. C., & de Grijs, R. 2002, *MNRAS*, 334, 646
- Kregel, M., van der Kruit, P. C., & Freeman, K. C. 2005, *MNRAS*, 358, 503
- Kuijken, K., & Gilmore, G. 1991, *ApJ Lett.*, 367, L9
- Lichtenberg, A. J. & Leiberman, M. A. 1983, *Regular and Stochastic Motion*, Springer-Verlag, New York.
- Malhotra, R. 1993, *Nature*, 365, 819
- Martinez-Valpuesta, I., Shlosman, I., & Heller, C. 2006, *ApJ*, 637, 214
- Mayer, L., Governato, F., & Kaufmann, T. 2008, *ArXiv e-prints*, 801, arXiv:0801.3845
- Merritt, D., & Sellwood, J. A. 1994, *ApJ*, 425, 551
- Misiriotis, A., & Athanassoula, E. 2000, *Dynamics of Galaxies: from the Early Universe to the Present*, 197, 69
- Miller, R. H. 1978, *ApJ*, 226, 81
- Murray, C. D., & Dehnen, W. 1999, *Solar System Dynamics*, Cambridge University Press, Princeton.
- Navarro, J. F., Frenk, C. S., & White, S. D. M. 1997, *ApJ*, 490, 493
- Ojha, D. K., Bienayme, O., Mohan, V., & Robin, A. C. 1999, *A & A*, 351, 945
- O'Neill, J. K., & Dubinski, J. 2003, *MNRAS*, 346, 251
- Preto, M., & Tremaine, S. 1999, *AJ*, 118, 25 32
- Quinn, T., Katz, N., Stadel, J., & Lake, G. 1997, *ArXiv Astrophysics e-prints*, arXiv:astro-ph/9710043
- Sellwood, J. A. 1980, *A & A*, 89, 296
- Sellwood, J., & Debattista, V. 2006, *ApJ*, 639, 868
- Sheth, K., et al. 2008, *ApJ*, 675, 1141
- Seth, A. C., Dalcanton, J. J., & de Jong, R. S. 2005, *AJ*, 129, 1331
- Springel, V., Yoshida, N., & White, S. D. M. 2001, *NewA*, 6, 79
- Springel, V. 2005, *MNRAS*, 364, 1105
- Tremaine, S., & Weinberg, M. D. 1984, *MNRAS*, 209, 729
- Valenzuela, O., & Klypin, A. 2003, *MNRAS*, 345, 406
- Wadsley, J. W., Stadel, J., & Quinn, T. 2004, *NewA*, 9, 137
- Valenzuela, O., Rhee, G., Klypin, A., Governato, F., Stinson, G., Quinn, T., & Wadsley, J. 2007, *ApJ*, 657, 773
- van der Kruit, P. C., & Searle, L. 1981, *A & A*, 95, 105
- Weinberg, M. D. 1985, *MNRAS*, 213, 451
- Weinberg, M. D., & Katz, N. 2007, *MNRAS*, 375, 425
- Widrow, L. M., Pym, B., & Dubinski, J. 2008, *ApJ*, 679, 1239
- Xilouris, E. M., Byun, Y. I., Kyla, S. N. D., Paleologou, E. V., & Papamastorakis, J. 1999, *A & A*, 344, 868
- Xue, X., et al. 2008, *ArXiv e-prints*, 801, arXiv:0801.1232
- Yochim, P., & Dalcanton, J. J. 2006, *AJ*, 131, 226
- Zemp, M., Stadel, J., Moore, B., & Carollo, C. M. 2007, *MNRAS*, 376, 273